Cell

Structural Basis for Actin Assembly, Activation of ATP Hydrolysis, and Delayed Phosphate Release

Kenji Murakami,[1,6] Takuo Yasunaga,[3] Taro Q.P. Noguchi,[4] Yuki Gomibuchi,[1] Kien X. Ngo,[4] Taro Q.P. Uyeda,[4] and Takeyuki Wakabayashi[1,2,5,*]

[1]Department of Biosciences, School of Science and Engineering
[2]Department of Judo Therapy, Faculty of Medical Technology
Teikyo University, Toyosatodai 1-1, Utsunomiya 320-8551, Japan
[3]Department of Bioscience and Bioinformatics, Faculty of Computer Science and Systems Engineering, Kyushu Institute of Technology, Ooaza-kawazu 680-4, Lizuka, Fukuoka 820-850, Japan
[4]Biomedical Research Institute, National Institute of Advanced Industrial Science and Technology, AIST Tsukuba Central 4, 1-1-1 Highashi, Tsukuba, Ibaraki 305-8562, Japan
[5]Department of Physics, School of Science, University of Tokyo, Hongo 7-3-1, Bunkyo-ku, Tokyo 113-0033, Japan
[6]Present address: Department of Structural Biology, Stanford University, Stanford, CA 94305, USA
*Correspondence: wakabayashi@nasu.bio.teikyo-u.ac.jp
DOI 10.1016/j.cell.2010.09.034

SUMMARY

Assembled actin filaments support cellular signaling, intracellular trafficking, and cytokinesis. ATP hydrolysis triggered by actin assembly provides the structural cues for filament turnover in vivo. Here, we present the cryo-electron microscopic (cryo-EM) structure of filamentous actin (F-actin) in the presence of phosphate, with the visualization of some α-helical backbones and large side chains. A complete atomic model based on the EM map identified intermolecular interactions mediated by bound magnesium and phosphate ions. Comparison of the F-actin model with G-actin monomer crystal structures reveals a critical role for bending of the conserved proline-rich loop in triggering phosphate release following ATP hydrolysis. Crystal structures of G-actin show that mutations in this loop trap the catalytic site in two intermediate states of the ATPase cycle. The combined structural information allows us to propose a detailed molecular mechanism for the biochemical events, including actin polymerization and ATPase activation, critical for actin filament dynamics.

INTRODUCTION

The actin-filament system is required in almost all cytoplasmic processes, including cell adhesion, motility, cellular signaling, intracellular trafficking, and cytokinesis. Although stable actin filaments (F-actin) are necessary during muscle contraction, the active turnover of filaments is required in many cell functions. Actin has two major domains separated by a nucleotide-binding cleft (Kabsch et al., 1990). The outer domain is divided into subdomains 1 and 2 and the inner domain into subdomains 3 and 4. All of the subdomains interact with the bound nucleotide. ATP is hydrolyzed at the rate of 1/3.3 s^{-1} following the elongation of filaments at the growing end of filaments (Blanchoin and Pollard, 2002), whereas the phosphate release is 100 times slower (Carlier and Pantaloni, 1986). As a result, newly polymerized filaments consist of stable ADP-Pi actin (abbreviated as F-ADP-Pi), whereas the older filaments contain mainly ADP actin (F-ADP), which disassembles more rapidly (Carlier and Pantaloni, 1986). Under physiological conditions, inorganic phosphate (Pi) binds to F-actin and reduces the critical concentration for polymerization (Rickard and Sheterline, 1986; Fujiwara et al., 2007). Actin dynamics also depends on the identity of the bound divalent cation, physiologically Mg^{2+}, associated with the bound nucleotide (Carlier et al., 1986).

Although a vast amount of biochemical data has been accumulated, the quest for a definitive and detailed molecular mechanism of the polymerization of monomeric actin (G-actin) to filamentous actin (F-actin) has been hampered by the inherent flexibility of actin filament. The flexibility has not allowed an atomic structure of F-actin to be determined. More than 50 atomic structures of G-actin bound with ATP or ADP have been determined since 1990 (Kabsch et al., 1990), but F-actin has been visualized to relatively moderate resolution either by three-dimensional (3D) image reconstruction from electron micrographs (Belmont et al., 1999) or modeling based on X-ray fiber diagrams (Holmes et al., 1990; Lorenz et al., 1993). The inherent flexibility of actin filaments hampers determination of atomic structure.

Recently, a new model of F-actin based on improved X-ray fiber diffraction analysis was reported (Oda et al., 2009). Oda et al. proposed that outer-domain movement upon assembly flattens the actin molecule in the polymer, similar to the case of the bacterial actin homolog MreB (van den Ent et al., 2001),

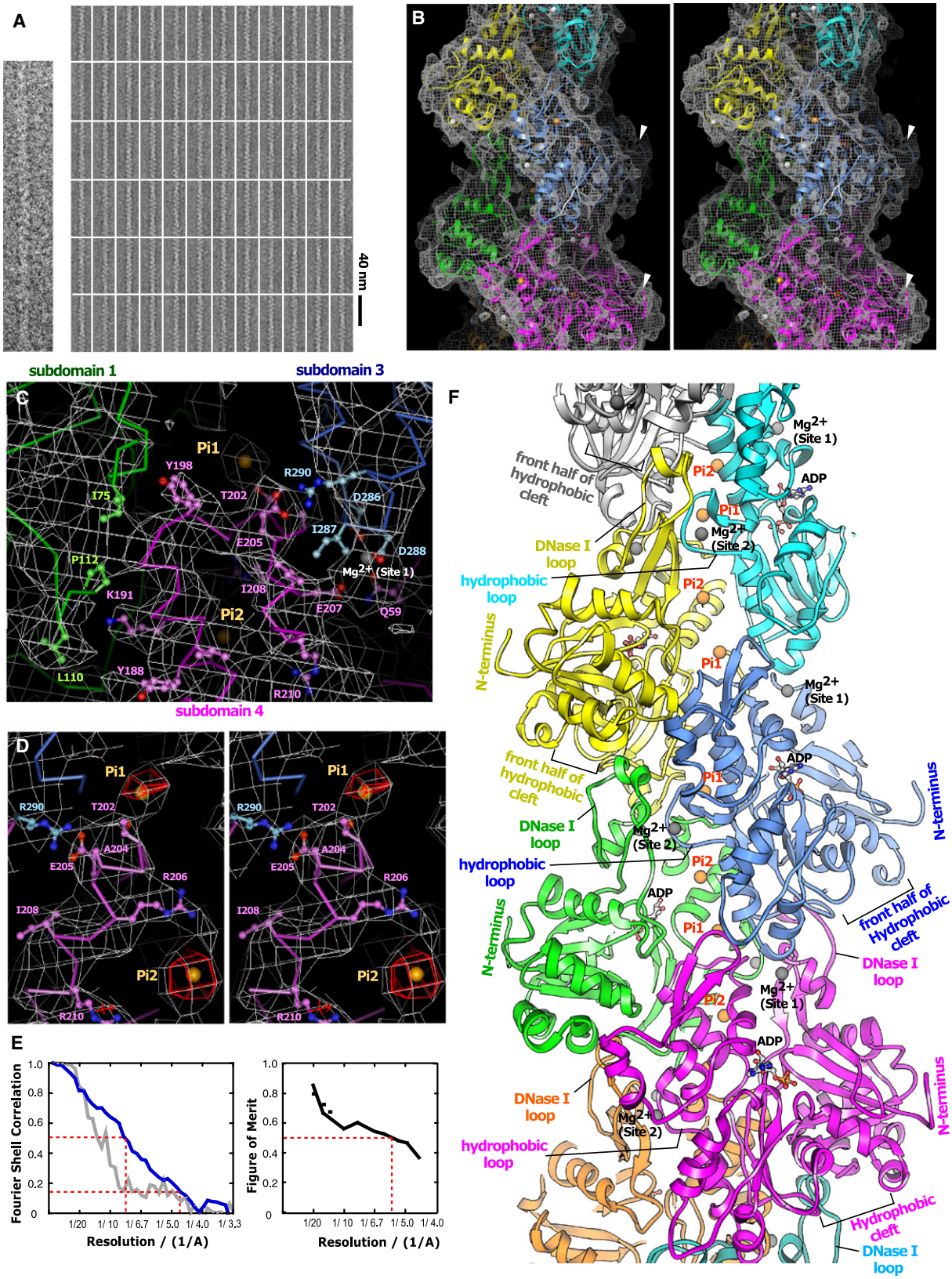
A
40 nm
B
subdomain 1
subdomain 3
C
Pi1
Y198
R290
T202
D286
I75
I287
E205
D288
P112
Mg2+ (Site 1)
K191
I208
Pi2
E207
Q59
L110
Y188
R210
subdomain 4
D
Pi1
R290
T202
A204
E205
R206
I208
Pi2
R210
E
Fourier Shell Correlation
Resolution / (1/A)
Figure of Merit
Resolution / (1/A)
F
Mg2+ (Site 1)
front half of hydrophobic cleft
Pi2
ADP
Pi1
Mg2+ (Site 2)
DNase I loop
hydrophobic loop
N-terminus
front half of Hydrophobic cleft
Hydrophobic cleft

and that the DNase I binding loop (DNase I loop) adopts an open loop conformation. However, the mechanism of ATP hydrolysis and its coupling with actin assembly remains poorly understood.

Here, we present cryo-electron microscopic (cryo-EM) data in which single-particle analysis has been applied to short and relatively straight stretches of filaments, with Pi added in the millimolar range (similar to the intracellular Pi concentration), to further minimize filament flexibility (Nonomura et al., 1975). The quality of the cryo-EM images was further refined as described in the Experimental Procedures.

The resolution of the final reconstruction was estimated to be ~5 Å (Fourier shell correlation [FSC] of 0.143 at 4.7 Å, a criterion according to Rosenthal and Henderson [2003]) or ~8 Å (FSC of 0.5 at 7.8 Å, a traditional criterion), and some of the α-helical backbones and large side chains can be directly observed. This indicates that the data quality was sufficient to visualize the structural changes upon polymerization and allowed us to build a quasi-atomic model of F-actin (F-ADP+Pi). Putative Mg^{2+}-binding sites and Pi-binding sites of F-actin, which play an important role in actin assembly, were identified in the EM map, and the proline (Pro)-rich loop (residues 108–112) was observed to adopt a more bent configuration that would trigger a phosphate-releasing pathway. Crystal structures of G-actin with mutations in this loop, in which the ATPase activity was increased or decreased, further revealed the region required for Pi release (the so-called back-door region; Wriggers and Schulten, 1999) and the atomic details of the mechanism of ATP hydrolysis. The combined structural information sheds new light on the coupling mechanism of ATP hydrolysis and F-actin assembly.

RESULTS

Overall Structure of Actin in a Filament

The 3D cryo-EM structure was reconstructed from segments containing 26 actin molecules (Figure 1B). Approximately 8000 actin molecules from zero energy-loss cryo-EM images of actin filaments in the presence of phosphate (Figure 1A) contributed to the final EM map (Figure 1 and Figure S1 available online). A quasi-atomic model (Figures 1B and 1D) was constructed by refining the initial F-actin model consisting of 26 G-ADP actin molecules (Rould et al., 2006) to obtain a good fit into the EM density map (see Figure S1, Movie S1, Movie S2, and Figure 1E for FSC and figure-of-merit [FOM] plots). The resolution of the structure of F-actin appeared to be nonuniform depending on the regions (Figure 1E). In the region where three actin molecules interact within the filament, the quality of EM map was better (Figure 1E) and the backbone structure of α helices 5 and 6 (h5, residues 183–196; h6, residues 207–216) and the Thr-rich loop (residues 197–204) could be clearly resolved, allowing the assignment of some large side chains such as Lys191, Tyr198, and Arg206 (Figures 1C and 1D). Although no β structure could be directly visualized, most α helices and loops defined in Figure 2C could be assigned. The N-terminal segment (residues 1–5), h0 (residues 41–48) in the middle of DNase I loop, and h7 (mobile helix: residues 226–230) were less clearly resolved but still allowed main-chain placement except for the h0 segment, which is disordered. The structural details are shown in Figures S1F–S1H.

Outer-Domain Rotation and Widening of Hydrophobic Cleft

In the F-actin structure, the relation between the two major actin domains is different from that in G-actin. The outer domain is found rotated in a swing-door manner by ~16° relative to the inner domain (Figure 2A). The pivoting point, Asp154 next to P loop 2, is located near the bound nucleotide, with two hinges: Gln137-Ala138 and Lys336-Tyr337 (Figures 2A and 2C). The axis of the rotation was oriented by ~40° relative to the filament helix axis (Figure 2A) and not vertical to the helix axis (Oda et al., 2009) (Figure S2). The outer-domain rotation enables the DNase I loop to fit in the rear half of the hydrophobic cleft (Figure 1F) so that it could reach Leu110, which can be clearly assigned in

Figure 1. Representative EM Density of Actin Filament

(A) An original zero energy loss cryo-EM image of actin filament on the left and a gallery of classified and averaged images of actin filament containing 26 molecules on the right. Although images were averaged after they were classified into 120 groups with 3° step rotation angles, a gallery shows only 72 projections with 5° step. Scale applies only for a gallery.

(B) Stereo pair of the density map of actin filaments (gray contours). The atomic model is also shown. Each actin molecule is represented by a different color. Phosphate and magnesium ions are shown in orange and white, respectively. White arrowheads indicate the N terminus.

(C) Density map (gray contours) for the intermolecular interface of actin filament. Orange and gray spheres indicate phosphate and magnesium ions, respectively. Residues involved in the intermolecular interactions were well resolved and are shown in ball and stick format.

(D) Stereo pair showing the densities of helix 6 (h6) in gray contours and rotated by 90° with respect to (C). The difference densities (EM map minus atomic model; red contours, 5σ) correspond to two phosphate ions (orange spheres) at the phosphate-binding sites 1 and 2.

(E) Fourier shell correlation (FSC) between two reconstructions after dividing the data into two halves (left). For the total structure (in gray), the FSC curve behaves less regularly, reflecting the nonuniform resolution depending on the regions. For the functionally important region, where the ternary interaction takes place, the map quality is better and the FSC curve behaves regularly and is suitable to estimate the resolution (in blue), which is ~8 Å (7.8 Å, FSC = 0.5 a traditional criterion) or ~5 Å (4.7 Å, FSC = 0.143, a criterion taking account of the effect of halving data; Rosenthal and Henderson, 2003). For its calculation, the region enclosed in a cosine-edged cylinder with a diameter of 36.4 Å and a height of 22.8 Å (covering ~44% of the whole molecular volume) was used. The estimated resolution is consistent with the observation that some α-helical backbones and large side chains were directly visible in the EM maps shown in (C) and (D). Figure of merit (FOM) was calculated from the Fourier transform of the EM density map and the atomic model in each resolution shell (Yonekura et al., 2003) (right). A shell FOM of 0.5 was used as a criterion to determine the resolution limit. The shell FOM was above 0.5 out to 6.0–7.0 Å resolution shell.

(F) Ribbon diagram of F-actin. Two phosphates (orange) and two Mg^{2+} (gray) located at intermolecular interface are shown in sphere format. Locations of the N terminus, hydrophobic cleft, hydrophobic loop, and DNase I loop are indicated. ADP is shown in ball and stick format. In all panels, the minus end (pointed end) of filament is upward.

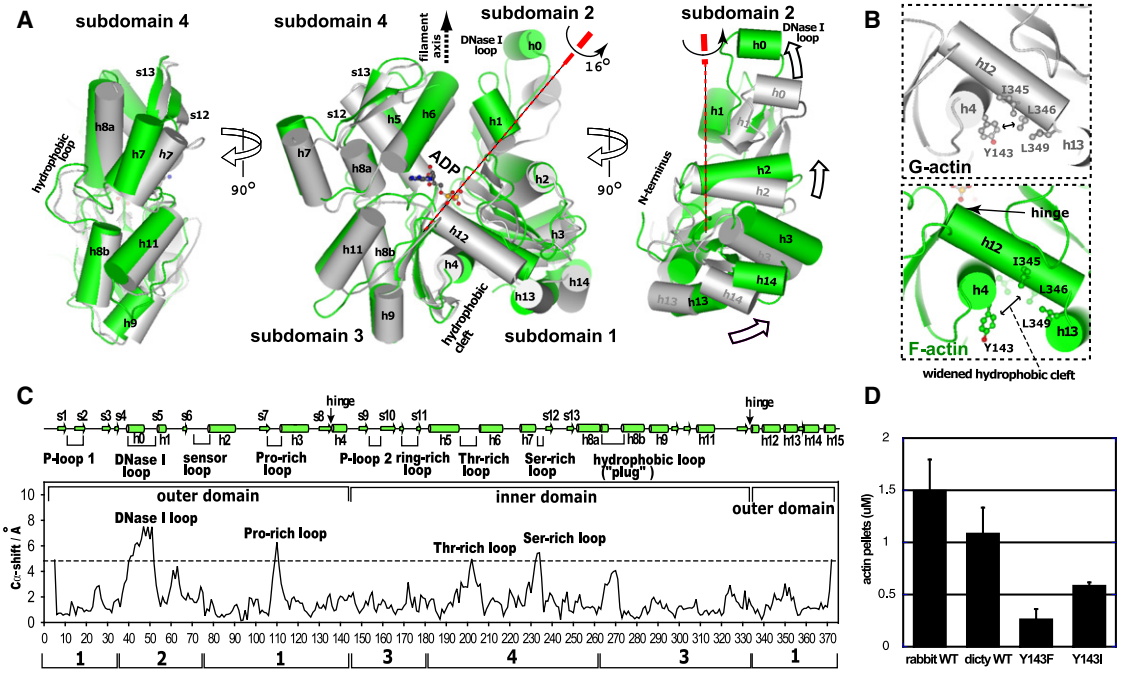

Figure 2. Comparison of F-Actin Structure with G-Actin Structure

(A) The inner domain of the G-actin (G-ADP) (gray; Otterbein et al., 2001) was superimposed onto that of actin filament (F-actin) (green). In the F-actin structure (F-ADP+Pi), the outer domain is rotated by ~16° relative to the inner domain. The rotation angle was determined using DynDom (Hayward and Berendsen, 1998). The bound ADP is shown in ball and stick format.

(B) The enlarged frontal view of the hydrophobic cleft in F-actin (green) and G-actin (gray). DNase I loop (not shown) fits in the rear half of hydrophobic cleft. The front half of hydrophobic cleft remains empty and widens. The double-headed arrows show that the distance betweenTyr143 and Leu346 is wider in F-actin compared with that in G-actin. The arrow indicates the hinge point of the outer-domain rotation.

(C) Root-mean-square deviation (rmsd) per residue between the molecules of F-actin and G-actin. For the calculation, each of the inner and outer domains was superimposed onto that of G-actin independently. The structure within each domain is essentially the same as that of G-actin. The conformational changes occur mainly in DNase I loop, Pro-rich loop, Thr-rich loop, mobile helix h7, and Ser-rich loop, all of which are involved in the intermolecular interfaces.

(D) Actin polymerization assay. Actin mutants (2.3 μM) were incubated at 25°C, ultracentrifuged, and analyzed by SDS-PAGE. The data represent mean values with standard errors of the actin pellets (n = 4).

the EM map, of the actin molecule on the minus-end side (Figure 1C and Movie S1). As a result of the outer-domain rotation (Figure 2A), the front half of the hydrophobic cleft is widened, making the side chain of Tyr143 more solvent exposed and increasing the distance between Tyr143 and Leu346 on the hydrophobic helix (h12) (Figure 2B). The importance of the front half of the hydrophobic cleft for polymerization is further highlighted by the fact that the *Dictyostelium* actin with Tyr143Phe mutation polymerizes poorly. The Tyr143Ile mutation, however, has only a small inhibitory effect on assembly (Figure 2D). This is consistent with the fact that the corresponding residue of the bacterial actin homolog MreB is Ile (van den Ent et al., 2001). The front half of the hydrophobic cleft is also a primary site for G-actin- and/or F-actin-binding proteins, which could regulate actin assembly by promoting or blocking the widening of the hydrophobic cleft. Indeed, small marine toxins such as kabirimide C and jaspisamide A (Klenchin et al., 2003), which bind to the front half of the hydrophobic cleft and sever actin filament, are sterically compatible with our F-actin structure. This may partially account for the inhibitory effect of modification of Cys374 with tetramethylrhodamine (TMR) on polymerizability (Otterbein et al., 2001).

Structural Changes in the Intermolecular Interface

Accompanying the domain rotation, the main-chain atoms shift more than 4.8 Å mainly in the loop regions (Figure 2C), which facilitates intermolecular interactions. This results in a buried surface area between three actin molecules of up to 7646 Å^2, which is a substantial increase compared to 2998 Å^2 for the crystal structure of G-ADP actin docked into the EM map without remodeling. At the interface of the three actins within the filament (Figures 1C and 1D and Figure 3A), the Thr-rich loop (containing Thr202 and Thr203) was remarkably different from that in G-actin (shown in gray in Figure 3A). Furthermore, the N-terminal part of h6 was shifted compared to that in G-actin (shown in gray in Figure 3A and Figure S1A) and possibly stabilized by a putative salt bridge of Glu205 with Arg290 of the upper molecule and the hydrophobic interaction of Ala204 and Ile208 with Ile287 of the upper molecule. The disruption of h6 is observed in the crystal structure of the actin-DNase I complex (Kabsch et al., 1990). Local reordering of the N-terminal part of h6 could provide a common binding site for actin-binding proteins, including actin itself, and could also help bind a magnesium ion (site 1 in Figure 3A) and two phosphate ions (Pi1 and Pi2, Figure 1D).

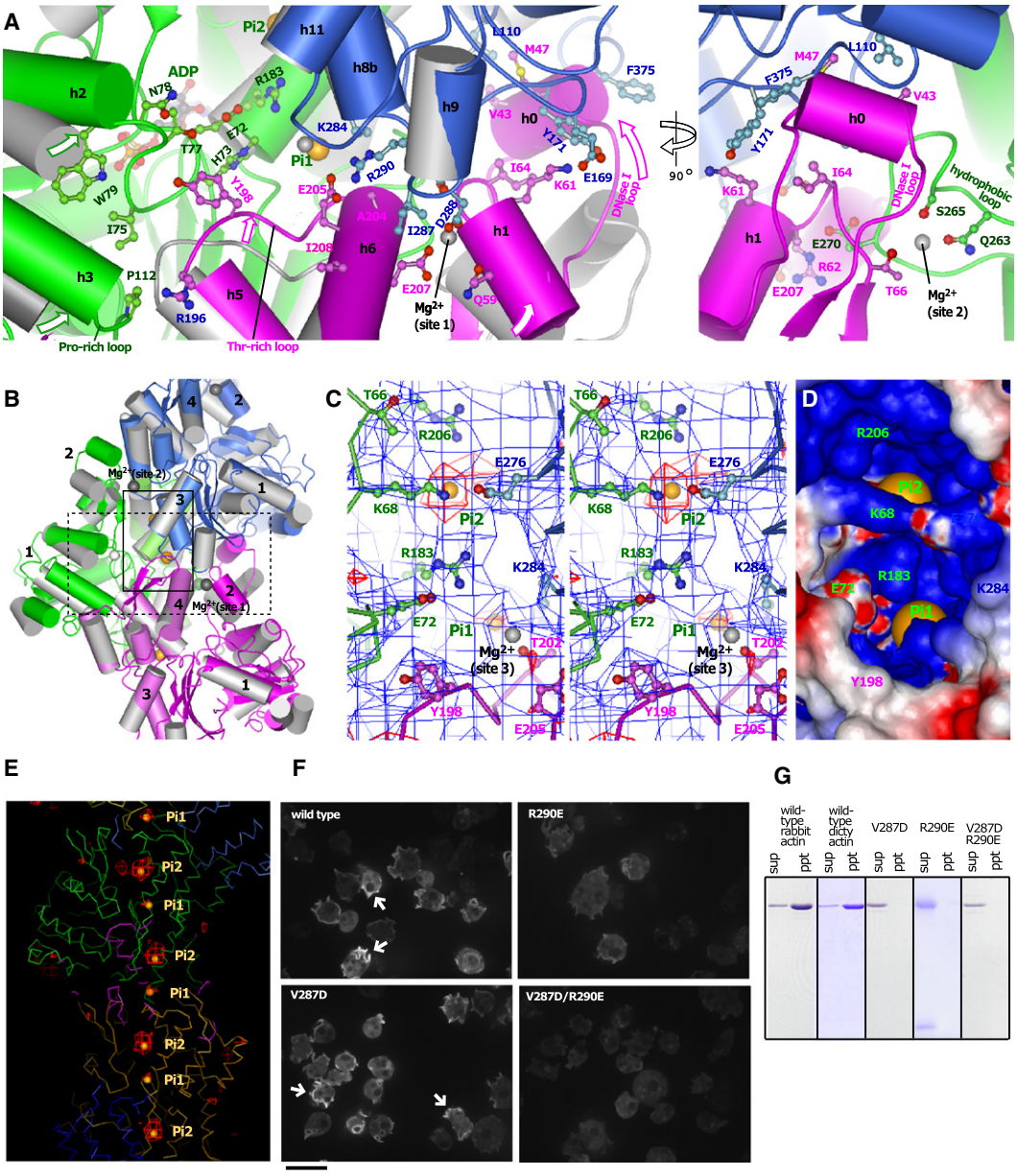

Figure 3. Intermolecular Interfaces of the Actin Filament

(A) Cartoon representation of the interfaces of actin filament. The structure of G-actin in gray (Otterbein et al., 2001) was superimposed onto each molecule of actin filament by fitting subdomain 3. Each of the actin molecules of F-actin is represented by a different color. The phosphates and Mg^{2+} are represented as orange and gray spheres, respectively.

(B) Cartoon representation of the actin filament. Actin subdomains are numbered. The areas enclosed with the dotted and solid rectangles are shown in (A) and (C), respectively.

(C) The stereo pair for the area around the phosphate-binding sites with the corresponding EM densities (blue contours) and the difference map (red contours, 5σ).

(D) Surface electrostatic potential in the same area as in (C). Two phosphate ions are surrounded by positive electrostatic potential.

(E) The difference map (EM map minus atomic model; red contours, 5σ) showing the two phosphate ions at sites 1 and 2.

(F) Confocal fluorescence micrographs of cells expressing GFP-fused actin. GFP-fused wild-type actin and GFP-fused V287D actin show more pronounced cortical accumulation, particularly at pseudopodia (arrows), than do GFP-fused R290E actin or GFP-fused V287D/R290E actin. All of the micrographs are shown without automatic contrast adjustment (exposure time: 2 s for GFP-fused wild-type actin and GFP-fused V287D, 4 s for GFP-fused R290E actin and GFP-fused V287D/R290E). The extent of polymerization of each actin mutant was assayed by quantifying the ratio of GFP-actin in insoluble fractions of cells treated with Triton to the total GFP-actin of cells treated with Triton: 0.35, 0.34, 0.21, and 0.13 for the GFP-fused wild-type actin, GFP-fused V287D actin, GFP-fused R290E actin, and GFP-fused V287D/R290E actin, respectively. Scale bar, 10 μm.

(G) Actin polymerization assay. Actin mutants (2.3 μM) were incubated at 25°C, ultracentrifuged, and analyzed with SDS-PAGE. The pellet (ppt) is 6.3-fold concentrated relative to supernatant (sup).

Table 1. Putative Phosphates and Magnesium Ions in F-Actin and Corresponding Sites in Crystal Structures of G-Actin

Sites in F-Actin		Peak Height[a]	Coordinating Residues in F-Actin	Corresponding Sites in G-Actin with the PDB Code
1	Pi (site 1)	5.2 σ	*R183*, *D184*, T202[b], K284	3CI5 (SO_4^{2-}), 2Q36 (SO_4^{2-}), 1YAG (SO_4^{2-}), 1D4X (SO_4^{2-}), 1YVN (SO_4^{2-}), 1NLV (SO_4^{2-}), 1NM1 (SO_4^{2-}), 1NMD (SO_4^{2-})
2	Pi (site 2)	5.9 σ	R183, R206	3CI5 (SO_4^{2-})
3	Pi (site 3)	4.8 σ	K238, R254	2A5X (TSA[c]), 2A42 (glycerol), 3CI5 (SO_4^{2-})
4	Mg^{2+} (site 1)	5.6 σ	D286, D288, E207, Q59	1NWK (Ca^{2+}), 2FXU (Ca^{2+}), 2VYP (Ca^{2+}), 2HF3 (Ca^{2+})
5	Mg^{2+} (site 2)	3.0 σ	Q263, S265, *T66*	2Q1N (Ca^{2+}), 2Q0U (Ca^{2+}), 2A5X (Ca^{2+}), 3EKS (Ca^{2+}), 2HF3 (Ca^{2+}), 2ASM (Ca^{2+}), 3EKU (Ca^{2+}), 2Q0R (Ca^{2+}), 2HF4 (Ca^{2+}), 3EL2 (Ca^{2+}), 2A5X (Ca^{2+})
6	Mg^{2+} (site 3)	3.6 σ	T202, E205	1YXQ (Mg^{2+}), 1J6Z (Ca^{2+})
7	Mg^{2+} (site 4)	6.3 σ	Q354, E361	1J6Z (Ca^{2+}), 1NWK (Ca^{2+}), 2VYP (Ca^{2+})
8	Mg^{2+} (site 5)	5.1 σ	D222, E316, E259	2HMP (Sr^{2+})

[a] Peak height in the EM difference map (EM density minus the atomic model).
[b] The residues in the longitudinally and obliquely located actin molecules are indicated in underline and italic, respectively.
[c] N,N,N-TRIMETHYL-3-SULFOPROPAN-1-AMINIUM.

This feature of h6 is supported by *Dictyostelium* mutants Val287Asp or Arg290Glu, which both polymerized poorly (Figure 3G), emphasizing the importance of Ile287 (Val287 in *Dictyostelium* actin) and Arg290 in the vertical interaction. In addition, these mutants exhibit more disperse distribution when fused to GFP in *Dictyostelium* cells, with the double mutant displaying a more prominent phenotype (Figure 3F).

Phosphate-Binding Loops and Shifted Sensor Loop

Both of two Pi-binding loops, P loop 1 (residues 13–16) and P loop 2 (residues 156–159), could be assigned (Figure 4B). They surrounded the densities that correspond to α- and β-phosphates of the bound nucleotide, with no evidence for any γ-phosphate density. The region, where the γ-phosphate is located in the ATP form, is occupied by bulk solvent (Figure 4B), indicating that F-actin has bound ADP in the ATPase site (Figure 4B). Similar to the majority of crystal structures of G-actin with ATP or ADP, the nucleotide-binding cleft (Nolen and Pollard, 2007) is closed. However, the P loop 1 encircles a low-density region (a bubble in the EM map; Figure S4A), suggesting that two strands, s1 (residues 8–11) and s2 (residues 16–18), might be dynamically deformed. This could allow accommodation of the outer-domain rotation. Consistent with this, NMR spectroscopy showed that residues 1–22, which include P loop 1, are mobile even in an F-actin state (Heintz et al., 1996).

The sensor loop (residues 71–77), which reflects the state of bound nucleotide of G-actin (Rould et al., 2006), adopts a conformation similar to that of G-ADP (Otterbein et al., 2001; Rould et al., 2006) (Figure 3A). Compared with G-ATP actin, Glu72 on the sensor loop moves upwards by 2 Å and closer to Arg183. This enables a putative salt bridge between Glu72 and Arg183, which stabilize F-actin, as Arg183 is also associated with two phosphate ions.

Magnesium- and Phosphate-Binding Sites of F-Actin

Actin is known to have several binding sites for cations and phosphates (Rickard and Sheterline, 1986; Carlier et al., 1986). Also, more than 50 crystal structures of G-actin have been determined, and magnesium-binding sites have been deduced (Table 1; Klenchin et al., 2006).

After several cycles of refinement of the atomic model, a difference map (EM density minus the atomic model) showed significant peaks, greater than 3σ, with > 90% confidence by t test applied to three independently reconstructed EM maps (Figure 3E and Figure S3). The three strongest peaks (σ-values 5.2, 5.9, and 4.8) in the positively charged region (Figures 3C and 3D) are assigned as Pi (HPO_4^{2-}) because Pi was the only major anion in the specimens. The phosphate-binding sites 1 and 3 (Table 1) are also observed in the crystal structure of G-actin, in which the sites are occupied by sulfate ions (SO_4^{2-}). The EM data also supported the five magnesium-binding sites out of seven found in the crystal structures (Klenchin et al., 2006). They have significant densities in the EM difference map, with the peaks being more than 3σ (Figure S3) and with > 90% confidence by the t test analysis. The FOM values increase when the ions are incorporated to the model. The peaks in the EM difference map were found in the same locations as the cations in the crystal structures of G-actin. Thus, the coordinating residues in the model are in essentially the same conformation as in the crystal structures of G-actin.

The resultant atomic model of F-actin (F-ADP+Pi) included 5 Mg^{2+} and 3 HPO_4^{2-} ions per actin protomer (Figure S3). Because Pi is located outside of the ATPase site, it is not designated as F-ADP-Pi.

Two phosphate ions and two Mg^{2+} ions bound to the inner domain appear to have a crucial role in the intermolecular interactions. Mg^{2+} ions at site 1 and 2 would mediate longitudinal and oblique interactions, respectively (Figure 3A and Figure S3A). This could explain the importance of Mg^{2+} for actin assembly (Laki et al., 1962; Carlier et al., 1986). Mg^{2+} at site 1 reinforces the vertical interaction through coordination with two acidic residues, Asp288 and Glu207 on the vertically adjacent molecule. It also interacts with Gln59 of the actin molecule on the plus-end side. Consequently, Mg^{2+} site 1 forms an intramolecular bridge between the subdomains 2 (Gln59) and 4 (Glu207), which keeps the nucleotide-binding cleft closed. The configuration of Mg^{2+} site 2 is similar to that found in crystal structures of G-actin with a Mg^{2+} coordination to Gln263 and Ser265 of the hydrophobic loop (right panel of Figure 3A). In the F-actin model, its unique position in the groove of the actin double helix and near

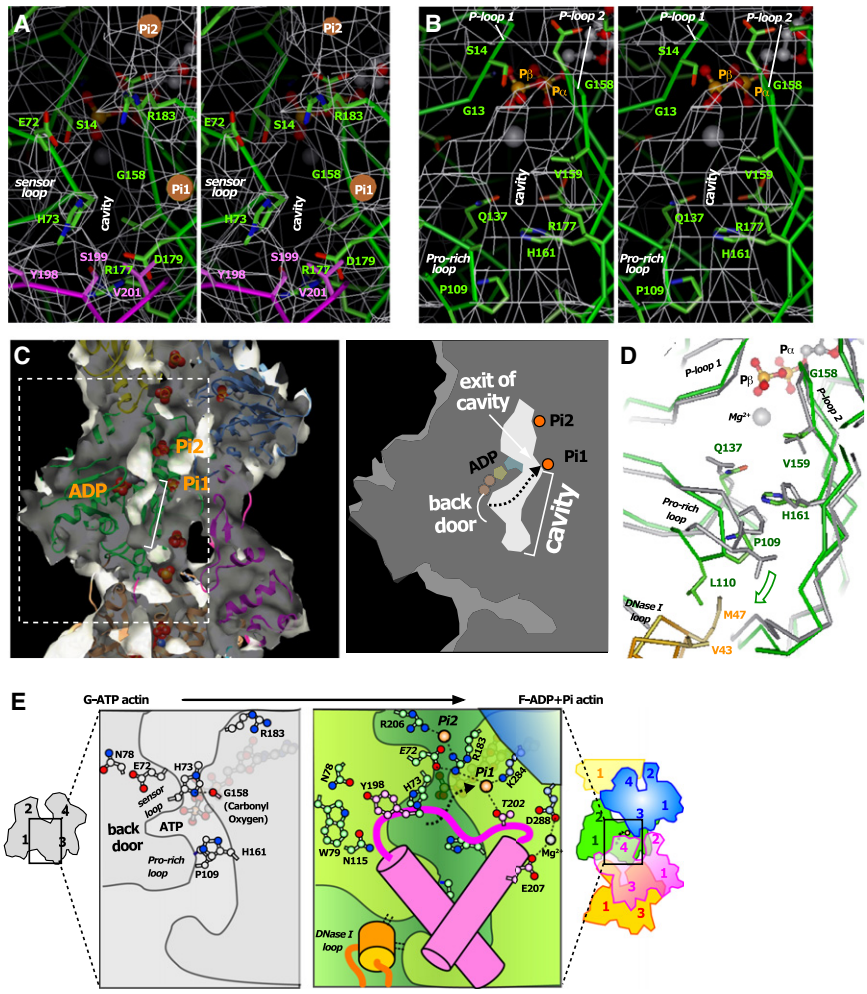

Figure 4. Structure around the Bound ADP in the Actin Filament

(A) The stereo pair for the structure around the exit of the phosphate-releasing cavity. The corresponding EM densities are shown in mesh format. Two inorganic phosphates are shown in orange spheres. The bound ADP is shown in ball and stick format.

(B) The stereo pair to show the phosphate-releasing cavity at the intermolecular interface of the actin filament. The Mg^{2+}-ADP is shown in ball and stick format, and magnesium ion is represented as a gray sphere.

(C) The vertically clipped view of the surface rendering of the EM map together with the schematic representation (right). The clipped surface is capped with a gray plane. The inside surface of the phosphate-releasing cavity can be seen in the top region, and the other side of the surface can be seen in the rest of the region. The bound ADP and phosphate ions (Pi1 and Pi2) are labeled and shown in solid sphere format. The cavity is indicated by a bracket. Its inside (white) and outside surface (gray) can be seen at the upper and lower part, respectively.

(D) The structure of the G-actin (gray) was superimposed onto the molecule of the actin filament (F-actin) (green) by fitting the P loop 2. In F-actin, the Pro-rich loop bends down more and the stacking interaction of Pro109 with His161 is disrupted.

(E) Summary of the conformational changes accompanied by the actin polymerization and ATP hydrolysis. Dotted straight lines indicate putative interactions. In F-actin (colored panel), the intermolecular cavity is formed along the groove between the outer and inner domains of the green molecule and is flanked by the subdomain 4 of the purple actin molecule. Because the phosphate-binding site 1 (Pi1) is located near the exit of the cavity, the hydrolyzed phosphate will be bound to this site before it escapes to the external solvent.

Thr66 of subdomain 2 promotes a contribution to the oblique interaction through the hydrophobic loop (right panel of Figure 3A).

Among three putative phosphate ions, two major peaks in the difference map (Pi-1 with 5.2σ and Pi-2 with 5.9σ; Figure 3E) are located near the center of the filament (Pi-1, ~1 Å from the filament axis; Pi-2, ~3 Å). The Pi at Pi-site 1 would stabilize the ternary interaction through interacting with Thr202 in the Thr-rich loop, Arg183 of the lateral molecule, and Lys284 of the upper molecule on the minus-end side (Figure 3C). The Pi at Pi site 2 is associated with Arg183 and Arg206 of the same lateral molecule (Figure 3C). Thus, Arg183 contributes to form two Pi sites. Of note, in the G-ATP state, the Arg183 side chain adopts a conformation unsuitable for either Pi site formation (Otterbein et al., 2001; Rould et al., 2006) (left panel of Figure 4E), which would suggest that polymerization and ATP hydrolysis may be required for the creation of the Pi-binding sites as seen in the F-actin model.

A Cavity as a Proposed Phosphate-Release Pathway

The phosphate release, as it occurs subsequent to actin polymerization, would be dependent on intrinsic properties of the F-actin. One key feature observed in the EM map is a cylindrical cavity (~18 Å long, ~6 Å in diameter) along the interdomain groove on the backside of the actin molecule, which was observed in the EM map (Figures 4A–4C and Figure S4) flanked by two additional actin chains (blue and purple in Figure 4E) and the β-phosphate of ADP (Figures 4B–4D; see also Movie S3). The cavity would be the only obvious route by which the hydrolyzed γ-phosphate could readily access the external solvent (Figure 4C and Figure S4). The Pi site 1, which is located near the exit of the cavity (Figure 4C), could constitute a possible intermediary binding site for the hydrolyzed γ-phosphate in a phosphate-release pathway (Figure 4E).

His73, which also flanks the cavity and is methylated in most eukaryotes, putatively changes side-chain configuration after polymerization. In the G-ATP state, the δ-nitrogen of His73 forms an interdomain H bond with the carbonyl oxygen of Gly158, thereby bridging two major domains (left panel of Figure 4E), whereas the H bond is likely to be disrupted in the F-actin. The imidazolic ring and the methyl group of methylated His73 are located near the phenolic ring of Tyr198 of

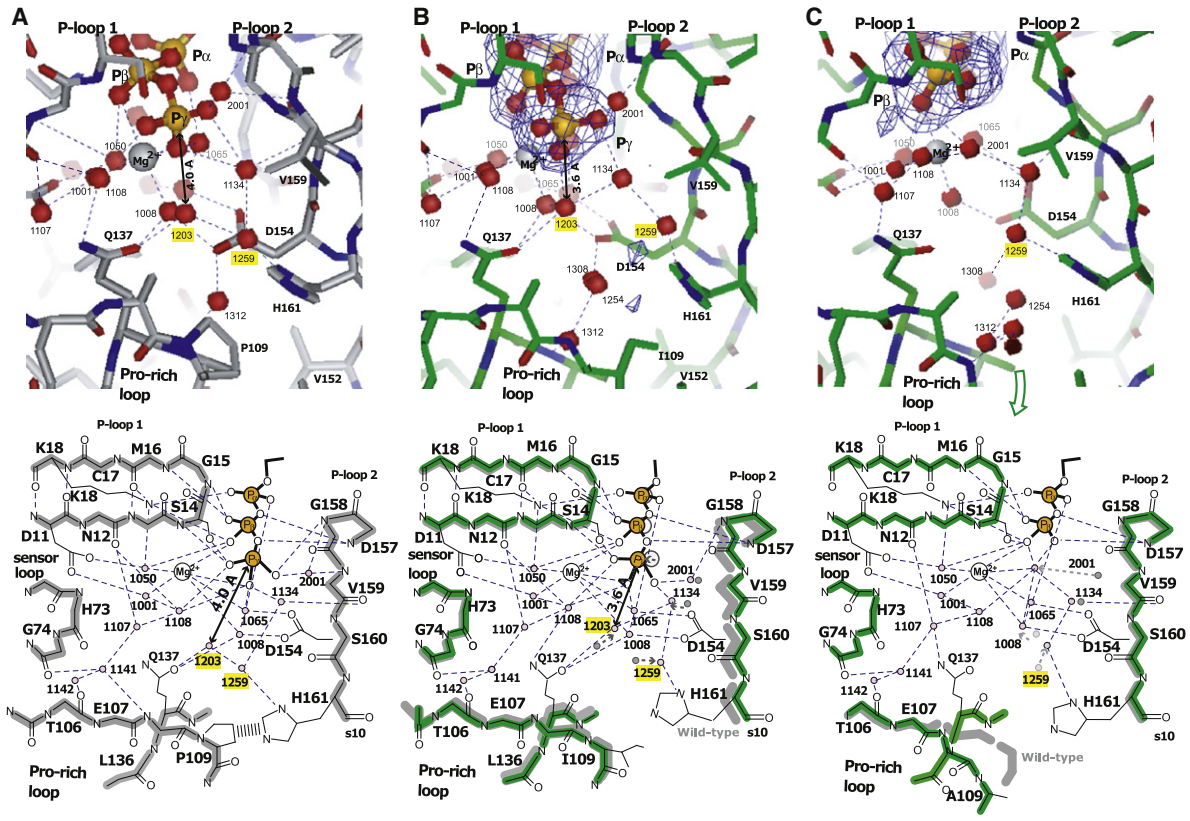

D

Summary of the Key Conformational Changes For ATP hydolysis in the Crystal Structures of Actin Mutants

		Wild Type (Ca^{2+})	P109I (Ca^{2+})	P109A (Ca^{2+})	Wild Type (Mg^{2+})	P109I (Mg^{2+})	P109A (Mg^{2+})
	PDB ID code	1C0F*	3A5O	3A5N	1NM1*	3A5M	3A5L
step 1	H-bond between waters 1203 and 1259	formed	**broken**	**broken**	formed	**broken**	
step 2	Distance between nucleophilic water and γ-phosphate	4.7 Å	4.4 Å	4.4 Å	4.0 Å	**3.6 Å**	
step 3	Nucleotide state	ATP / Ca^{2+}	ATP / Ca^{2+}	ATP / Ca^{2+}	ATP / Mg^{2+}	ATP / Mg^{2+}	**ADP / Mg^{2+}**
step 4	back door	closed	closed	half open	closed	closed	**fully open**
	sensor loop	down	down	down	down	down	**up**
	Pro-rich loop	up	up	down	up	up	**down**

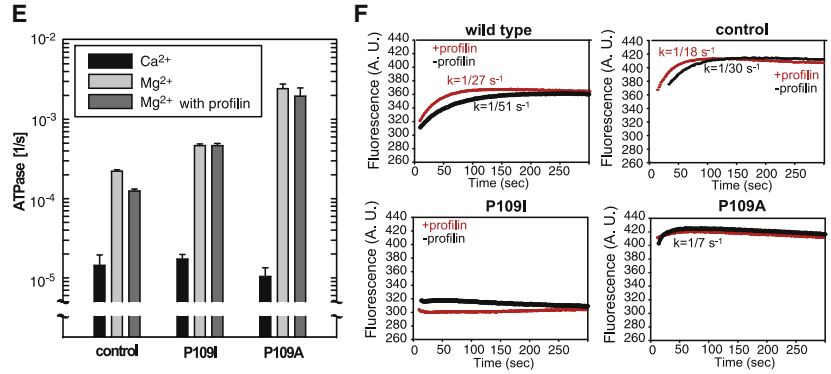

the obliquely adjacent molecule (Figure 4A) and could restrict the exit of the cavity (Figure 4E). The methylated His73 modulates access of the hydrolyzed γ-phosphate to the Pi site 1. Such a mechanism would explain reports of Pi release prior to polymerization when His73 is not methylated and Pi release from His73Ala-actin showing almost no lag time after polymerization (Nyman et al., 2002). Thus, we propose that the hydrolyzed γ-phosphate binds to the Pi-binding site 1 (Pi-site 1) and stabilizes the F-actin by reinforcing the ternary interaction before leaving actin filaments and that the methyl group of methylated His73 helps confine the Pi-release pathway.

Downward Bending of the Pro-Rich Loop

The EM map shows that the DNase I loop extends along the lateral molecule toward the upper molecule and the middle portion (h0, residues 41–48) of the DNase I loop associated with the Pro-rich loop (residues 108–112) of the upper molecule (right panel of Figure 3A). The exact conformation of the h0 segment of the DNase I loop could not be determined, but in our analysis, we have modeled it as a short α helix (Figure S1F), similar to that in the crystal structure of G-ADP actin (Otterbein et al., 2001). A large upward shift of this segment may explain why polymerization is inhibited by phosphorylation of Tyr53 (Liu et al., 2006): the phosphate group of phosphorylated Tyr53 could form H bonds with Lys61 and thus restricts the extendability of the DNase I loop (Baek et al., 2008).

It is most likely that residues in the middle portion of the DNase I loop are close to the Pro-rich loop; in particular, it forms an interaction with Leu110, of which the side-chain density was apparent in the EM map (Figures 1C). The Pro-rich loop, in turn, bends down toward the plus end. The stacking interaction of Pro109 with His161 observed in G-actin, however, is not possible in the F-actin model (Figures 4D and 4E). This is significant, as His161 and Gln137 both have been suggested to be involved in the ATP hydrolysis (Matsuura et al., 2000; Vorobiev et al., 2003), and the sensor loop and the Pro-rich loop (containing Pro109 and Pro112) constitute the back-door region, which has been suggested to control phosphate release (Wriggers and Schulten, 1999).

The importance of the Pro-rich loop was confirmed through a focused study of the Pro109 mutants using X-ray crystallography and ATPase assay (Figure 5 and Figure S5). Structural changes due to the mutations were observed mainly in the region around the bound nucleotide and h6, with no outer-domain rotation being observed.

In the structure of wild-type actin, a water molecule (Wat1203) is H-bonded to the ε-oxygen of Gln137, which renders it nucleophilic. However, a nucleophilic in-line attack on γ-phosphate would not occur (Matsuura et al., 2000; Vorobiev et al., 2003), as that water is too distant from the γ-phosphate (4.0 Å). The δ-nitrogen of His161 coordinates with another water molecule (Wat1259 in Figures 5A–5C), which, in turn, forms an H bond with the nucleophilic water and thus constrains its position (Figure 5A). In Pro109Ile-actin, His161 has no partner for stacking (Figure 5B), and the imidazolic ring of His161 is rotated by ~12°, which disrupts the H bond network between His161 and the nucleophilic water (Figure 5B). As a consequence, the nucleophilic water is found closer to the γ-phosphate (3.6 Å), but ATP hydrolysis does not occur (Figures 5B and 5E), presumably because the back door is still closed, likely due to a hydrophobic interaction of the introduced Ile109 with Val163 and Ile175. However, in Pro109Ala mutant where His161 still has no partner for stacking, the Pro-rich loop is found bent further downward by 1.8 Å (Figure 5C), with a shift in the main chain of Ala109 and Leu110, and no density for γ-phosphate is observed. The sensor loop is shifted upward in a manner similar to that in the F-ADP+Pi model or in G-ADP crystals (Otterbein et al., 2001; Rould et al., 2006). This indicates that the ATP added to the crystallization specimens is hydrolyzed with subsequent γ-phosphate release (Figure 5C). The ATPase activity of the Pro109Ala mutant in the presence of Mg^{2+} increased by ~10-fold under nonpolymerizable conditions compared to control actin (1/424 s^{-1} versus 1/4510 s^{-1}), whereas the activity of Pro109Ile actin was increased by ~2-fold (1/2159 s^{-1} [Figure 5E]). Using ethenoATP, the nucleotide exchange rate of Pro109Ala-actin was shown to be 40 times faster (1/7 s^{-1}) than the hydrolysis rate (Figure 5F). Taken together, these data indicate that the downward bending of the Pro-rich loop is the key prerequisite for ATP hydrolysis rather than the outer-domain rotation, which assists the bending of the Pro-rich loop during polymerization (Figure 6).

Mechanism of ATP Hydrolysis Based on X-Ray Crystallography

In the catalytic site of the G-actin structures, an extensive network of water molecules can be observed, which is stabilized through interactions with the P loop 1, the P loop 2, the sensor

Figure 5. Atomic Details of the Water-Mediated Hydrogen-Bonding Network of Crystal Structures of Actin Mutants in the Presence of Mg^{2+}

(A–C) Atomic details of the structure in the presence of Mg^{2+}. The region surrounding the bound nucleotide in wild-type actin and actin mutants is shown together with their schematic figures. (A) Wild-type actin (PDB ID code 1NM1), (B) P109I actin, and (C) P109A actin. All actin mutants were crystallized as complexes with gelsolin segment 1 (see Extended Experimental Procedures for details). The numbering of water molecules for wild-type actin is changed for easier comparison with mutant actins. Water molecules are shown in red spheres. Dotted lines indicate putative H bonds. The labels of the nucleophilic water (WAT1203) and the key water molecule (WAT1259) are highlighted in yellow. In the crystal structure of P109A actin (C), the Pro-rich loop bends downward more and the back door is opened (indicated by an arrow). ADP hydrolyzed from added ATP was observed. An omit-annealed $F_o - F_c$ map around the bound nucleotide is shown (blue contour), confirming the nucleotide state.

(D) Summary of the crystallographic studies. Asterisks indicate structures published previously. Atomic details of the structure in the presence of Ca^{2+} are shown in Figure S5.

(E) ATPase activities of actin mutants. E205A/R206A/E207A mutations were added into each of the actin mutants to make them polymerization incompetent (Noguchi et al., 2007) to exclude the effect of polymerization on ATPase activation. Each of the data points represents a mean value with a standard error (n = 4).

(F) Exchange kinetics of ethenoATP with G-ATP in the presence of Mg^{2+}. The rate is 1/30 s^{-1} and 1/7 s^{-1} for control actin (with E205A/R206A/E207A mutations) and P109A actin, respectively. Profilin accelerates the rates of both actins to the same extent.

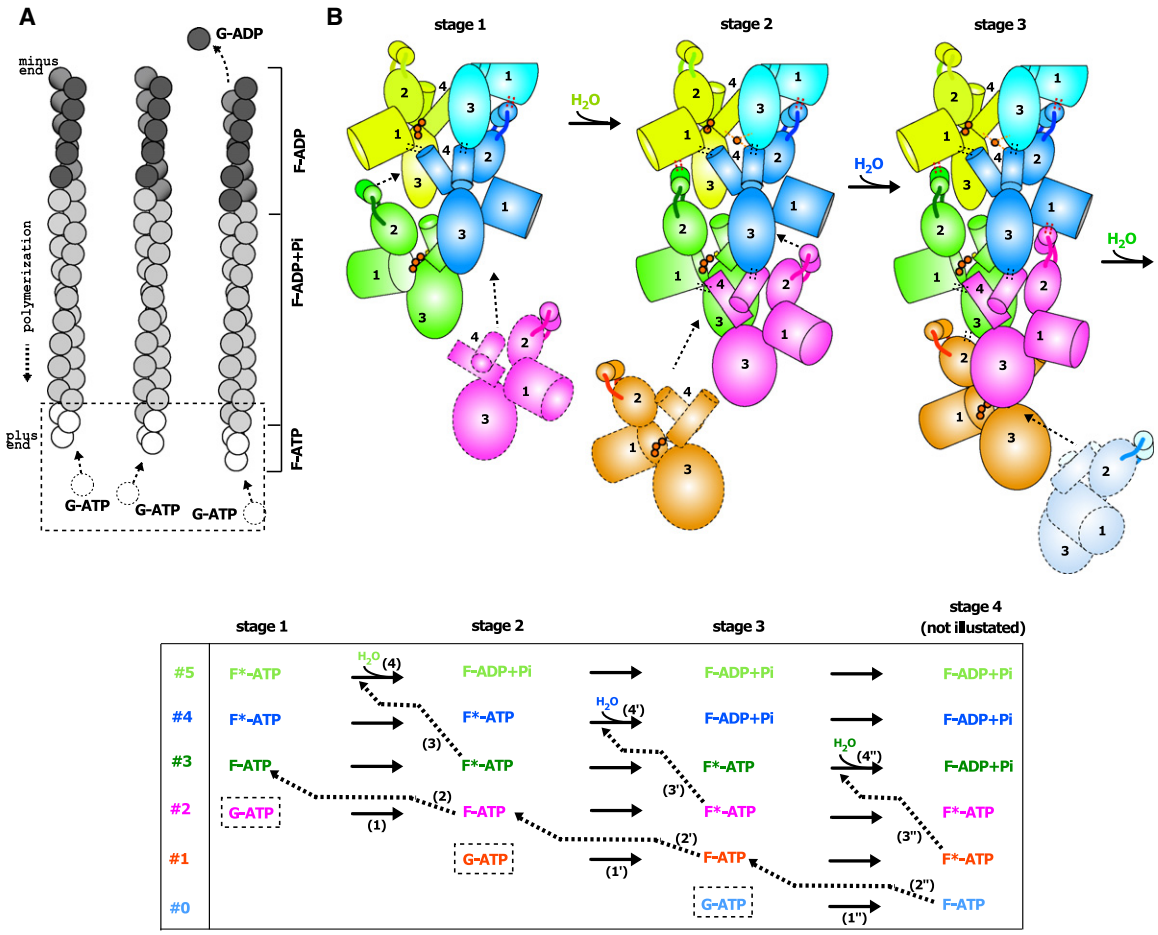

Figure 6. Proposed Model for Actin Polymerization

(A) Schematic diagram of actin polymerization. At steady state, actin monomers come on the filament at the plus end as G-ATP-actin (colored in white). After they are incorporated into the filament, ATP is hydrolyzed, forming an intermediate F-ADP+Pi (colored in gray) and then ADP-actin (colored in dark gray).

(B) Proposed model for actin polymerization at a plus end (downward elongation). Each actin molecule, with four subdomains being numbered, is represented by a different color. The phosphate moieties of the bound nucleotides and the hydrolyzed γ-phosphates are shown in orange spheres. The subdomain 4 is represented by two cylinders corresponding to helices h5 and h6. In this model, polymerization and ATP hydrolysis proceed in four steps as described in the text. This model implicates that the actin filament has at least three actin molecules in an F-ATP state on the plus end (ATP cap) and that the activation of ATPase does not occur in a trimer (a proposed nucleus for elongation).

loop, and the Pro-rich loop (Figures 5A–5C). Two water molecules, Wat1203 and Wat1259, which change their positions depending on the introduced mutation, could be critical in the function of the ATPase cycle in the presence of Mg^{2+}. We propose a four-step mechanism for the ATPase cycle (see Movie S4). First, by polymerization (or Pro109Ala mutation), the stacking interaction of His161 is lost, and the water-mediated (Wat1259) H bond between the nucleophilic water (Wat1203) and His161 is disrupted, with a back door being half open, allowing a shift in the position of the nucleophilic water. Second, the nucleophilic water (Wat1203) moves closer to the γ-phosphate. Third, the water attacks the ATP, which then is hydrolyzed to ADP and Pi. Fourth, the sensor loop shifts upward and facilitates the Pi release to the Pi-release cavity by fully opening the back-door. The proposed mechanism is supported by the conservation of key residues for ATPase activation (Pro109, Leu110, His161, and residues of two P loops [residues 13–16 and 156–159]) (Figure S5B). Figure 5D summarizes how ATPase activity correlates with the states of the key water molecules, the back door, and nucleotide.

In the presence of Ca^{2+}, ATPase activity is low (Figure 5E). The second step of ATPase cycle is slow because the water molecule Wat1108 is coordinated with Ca^{2+} ion keeping the nucleophilic water Wat1203 away from the γ-phosphate (4.4 Å) (see Figure S5A for details). This explains, in part, the differences between Ca^{2+}-actin and Mg^{2+}-actin in their dynamic polymerization properties (Carlier et al., 1986).

DISCUSSION

Rotational Flexibility of Outer Domain

One of the apparent structural changes in actin observed in the F-actin model compared to G-actin is a pronounced rotation of the outer domain in a swing-door manner. Such a rotation was

reported recently with the outer-domain rotation around the axis perpendicular to the actin helix axis, a propeller-like twisting (Oda et al., 2009) (Figure S2A). The observed apparent rotation in the F-actin model is, however, different, with the rotation axis oriented by 40° relative to the filament axis (Figure 2A). This rotation could be described as two perpendicular rotations, roughly propeller-like twisting and scissor-like closing. The apparent difference between the two studies may be due to the torsional and/or bending flexibility of actin filaments and absence of added Pi in the sample used to obtain the fiber diffraction data. Of note, the orientation of the outer domain is variable even among the crystal structures of G-actin (~10°), but this flexibility does not trigger ATP hydrolysis, suggesting that more substantial changes such as these shown in this work are required for ATPase activation to promote the downward bending of the Pro-rich loop, a key prerequisite for triggering ATPase activity.

How Polymerization Triggers ATP Hydrolysis

At the heart of the G-actin to F-actin dynamics lies the question how polymerization triggers ATP hydrolysis. We propose a detailed model for polymerization based on the F-actin model, outlined in Figure 6B and Movie S5. A newly incorporated molecule (#2 magenta) enables the outer-domain rotation of the penultimate actin molecule (#3 green). The other oblique interaction between the penultimate actin and the neighboring actin molecule (#4 blue) helps to orient the subdomain 2 of the penultimate actin so that its DNase I loop (the cylinder tethered to subdomain 2 in Figure 6B) reaches out upward. The middle portion of the DNase I loop fits in the rear half of the hydrophobic cleft, where the middle portion associates with the Pro-rich loop of the molecule on the minus-end side (#5 in yellowish green). This interaction induces the downward shift of Pro-rich loop and triggers ATP hydrolysis. The back door becomes fully open, and Pi is released to the Pi-release pathway (stage 2 in Figure 6B). Thus, the interaction of the DNase I loop with the Pro-rich loop is the key step to couple actin assembly with ATPase activation. These results explain why actin with a nicked DNase I loop polymerizes poorly (Khaitlina et al., 1993).

Hydrolyzed γ-phosphate binds to the Pi site 1 and reinforces the ternary interaction. Phalloidin, which binds to the site (Lorenz et al., 1993) near the Pi site 1 and slows the Pi release to the external solvent (Dancker and Hess, 1990), appears to mimic and/or reinforce the function of Pi. Unlike phalloidin, Pi can reversibly dissociate from the sites at low Pi concentrations, resulting in weakened intermolecular interactions.

In summary, the EM map and resulting quasi-atomic model of F-ADP+Pi show intricate intermolecular interfaces and binding sites for Pi and Mg^{2+} that allow proposal of a molecular mechanism of ATP hydrolysis upon actin assembly and delayed Pi release, in which the Pro-rich loop has a central role in coupling polymerization with ATP hydrolysis.

EXPERIMENTAL PROCEDURES

Electron Microscopy and Image Processing

Actin was prepared from rabbit skeletal muscle (Spudich and Watt, 1971). Actin filaments were prepared in solution containing 50 mM NaCl, 5 mM $MgCl_2$, 0.025 mM ATP, 10 mM sodium phosphate [pH 7.4], 0.05%NaN_3, and 0.7 mM DTT at room temperature (25°C). Zero energy loss cryo-EM micrographs were recorded at 200 kV (Hitachi EF-2000 with a cold field emission gun and an in-column energy filter) with a low-noise, high-sensitivity, and high-resolution CCD camera (Yasunaga and Wakabayashi, 2008) with electron dose of 15–20 $e^-/Å^2$, a nominal magnification of 100–110 k, and underfocus values of 1–1.5 μm. High-coherence beam generated by cold field emission gun was useful to minimize the image blurring due to underfocusing. The CCD camera with an epitaxially-grown scintillator (Yasunaga and Wakabayashi, 2008) helped collect images with high resolution. All of the images were analyzed with a pixel size of 2.28 Å with EOS software (Yasunaga and Wakabayashi, 1996). Images were segmented to contain 26 actin molecules and classified into 120 groups with 3° step rotation angles and were treated as single particles (Narita et al., 2001; Narita and Maéda, 2007). In the resultant 3D image, noncrystallographic helical symmetry was determined with cross-correlation analysis. Finally, the 14 actin molecules on the minus-end part in the EM map were averaged after fitting each other using SPIDER (Frank et al., 1996). The noncrystallographic helical symmetry with a 166.48° rotation and a 27.3 Å translation along the filament axis was used.

Model Building and Refinement

The initial model consisting of 26 G-ADP actin molecules (Rould et al., 2006) was manually fitted to the EM density using O (Jones et al., 1991). The refinement was performed using spatially restricted molecular dynamics (Noda et al., 2006). EM densities were treated as added pseudo-potential so that atoms tended to be retained in higher-density regions of the EM map. Throughout the refinement, the validity of the atomic model was checked with the real-space R factor with O (Jones et al., 1991) and the program pdbRhoFit (Yasunaga and Wakabayashi, 1996), which sums up the density of the EM map where the atoms are located. The degree of fit of the atomic model to the EM density was also accessed by calculating FOM from the Fourier transforms of the EM map and the atomic model (Yonekura et al., 2003). Manual model rebuilding using O (Jones et al., 1991) and refinement using steered-molecular dynamics were performed iteratively to produce the final model.

Crystallization and Structural Determination

Dictyostelium actin mutants were expressed and purified, as described previously (Noguchi et al., 2007), with slight modifications. To minimize the effect of polymerization on biochemical assays, E205, R206, and E207 were mutated to Ala so that actin becomes nonpolymerizable (Noguchi et al., 2007). Crystals of the complex of actin mutant (P109I/E205A/R206A/E207A) with gelsolin segment 1 in the Ca^{2+} state were obtained by hanging drops containing 13% PEG3550, 130 mM LiCl, 100 mM MES [pH 7.0], 0.2 mM $CaCl_2$, 0.5 mM DTT, 0.2 mM ATP, and 0.2 mM AMP-PNP. To obtain crystals in the Mg^{2+} state, 10 mM $MgCl_2$ and 0.5 mM EGTA were added before the crystallization. Crystals of the complex of another actin mutant (P109A/E205A/R206A/E207A) with gelsolin segment 1 were obtained in a similar manner. Crystals were cryoprotected with glycerol or ethylene glycol and then flash cooled in liquid nitrogen. Data were collected at Photon Factory (KEK, Japan). The structures were solved by molecular replacement (Storoni et al., 2004) using *Dictyostelium* wild-type actin (Matsuura et al., 2000) as an initial model. The models were rebuilt and refined using O (Jones et al., 1991) and Refmac5 (Collaborative Computational Project, Number 4, 1994).

Polymerization Assays

Each actin mutant (2.3 μM) was incubated in 150 mM NaCl, 20 mM imidazole-HCl (pH 7.0), 3 mM $MgCl_2$, 10 μM $CaCl_2$, and 1 mM ATP for 30 min at 25°C, ultracentrifuged, and analyzed by SDS-PAGE.

In Vivo Optical Microscopy

In vivo copolymerization of mutant actin with wild-type actin was assayed by quantifying GFP-actin. In brief, *Dictyostelium* cells expressing GFP-fused wild-type or mutant actin were grown in HL5. In the mid log phase of growth, the culture medium was replaced with lysis buffer containing 20 mM HEPES (pH 7.4), 50 mM NaCl, 2 mM $MgCl_2$, 1 mM EGTA, 0.5% Triton X-100, and

protease inhibitors. After 1 min, the soluble and insoluble fractions were separated and subjected to western blotting analysis using anti-GFP antibodies.

Assay of ATPase Activity and Nucleotide Exchange Rate

The ATPase activity of G-actin was measured as described previously (Saeki et al., 1996) in 10.7 μM actin mutant, 10 mM Tris-HCl (pH 7.5), 0.2 mM $CaCl_2$, 0.5 mM DTT, and 0.2 mM ATP at 25°C. To measure the activity for the Mg^{2+} state, 0.2 mM $MgCl_2$ and 0.3 mM EGTA were added before the measurement. E205A/R206A/E207A mutations were added to make the mutant polymerization incompetent (Noguchi et al., 2007) and exclude the effect of polymerization on ATPase activation. Nucleotide exchange was measured by fluorometry of the ethenoATP incorporated to G-actin (340 nm excitation, 410 nm emission). The experiments were performed with 2 μM actin in the presence or absence of 0.5 μM *Dictyostelium* profilin I. The reaction was initiated by diluting the actin solution (10 mM Tris-HCl [pH 7.5], 0.2 mM $CaCl_2$, 0.5 mM DTT, 0.2 mM $MgCl_2$, 0.3 mM EGTA, and 1 μM ATP) into a buffer containing 20 μM ethenoATP.

Figure Preparation

Figures were prepared using MOLMOL (Koradi et al., 1996) and Chimera (Pettersen et al., 2004).

ACCESSION NUMBERS

Atomic coordinates and structure factors have been deposited in the Protein Data Bank under accession codes 3A5L, 3A5M, 3A5N, and 3A5O. The accession code for actin filament structure is 3G37.

SUPPLEMENTAL INFORMATION

Supplemental Information includes Extended Experimental Procedures, five figures, three tables, and five movies and can be found with this article online at doi:10.1016/j.cell.2010.09.034.

ACKNOWLEDGMENTS

We thank Dr. Murray Stewart (MRC Lab. Mol. Biol., Cambridge) for discussions and advice on crystallography; Dr. Ralph Davis and Dr. Karl-Magnus Larsson (Stanford University) for critical reading of the manuscript; Dr. Akihiro Narita for his contribution to this work at the early stages; Dr. Soichi Wakatsuki and colleagues at Photon Factory, KEK for data collection at the synchrotron site; Dr. Koji Yonekura for the program to calculate a figure of merit; Dr. Hideo Higuchi for fluorometry; and Yuji Tuji, Akito Tominaga, Ryuta Mikawa, and Harumi Kiuchi for assistance with crystallography and/or biochemical experiments. This work was supported by grants from Human Frontier Science Program and Grant-in-Aid for Scientific Research on Priority Areas (Bio-supramolecule) from the Ministry of Education, Science, Technology, and Sports of Japan to T.W. and a grant from SENTAN, JST to T.Q.P.U.

Received: January 13, 2010
Revised: May 10, 2010
Accepted: September 1, 2010
Published: October 14, 2010

REFERENCES

Baek, K., Liu, X., Ferron, F., Shu, S., Korn, E.D., and Dominguez, R. (2008). Modulation of actin structure and function by phosphorylation of Tyr-53 and profilin binding. Proc. Natl. Acad. Sci. USA *105*, 11748–11753.

Belmont, L.D., Orlova, A., Drubin, D.G., and Egelman, E.H. (1999). A change in actin conformation associated with filament instability after Pi release. Proc. Natl. Acad. Sci. USA *96*, 29–34.

Blanchoin, L., and Pollard, T.D. (2002). Hydrolysis of ATP by polymerized actin depends on the bound divalent cation but not profilin. Biochemistry *41*, 597–602.

Carlier, M.F., and Pantaloni, D. (1986). Direct evidence for ADP-Pi-F-actin as the major intermediate in ATP-actin polymerization. Rate of dissociation of Pi from actin filaments. Biochemistry *25*, 7789–7792.

Carlier, M.F., Pantaloni, D., and Korn, E.D. (1986). Fluorescence measurements of the binding of cations to high-affinity and low-affinity sites on ATP-G-actin. J. Biol. Chem. *261*, 10778–10784.

Collaborative Computational Project, Number 4. (1994). The CCP4 suite: programs for protein crystallography. Acta Crystallogr. D Biol. Crystallogr. *50*, 760–763.

Dancker, P., and Hess, L. (1990). Phalloidin reduces the release of inorganic phosphate during actin polymerization. Biochim. Biophys. Acta *1035*, 197–200.

van den Ent, F., Amos, L.A., and Löwe, J. (2001). Prokaryotic origin of the actin cytoskeleton. Nature *413*, 39–44.

Frank, J., Radermacher, M., Penczek, P., Zhu, J., Li, Y., Ladjadj, M., and Leith, A. (1996). SPIDER and WEB: processing and visualization of images in 3D electron microscopy and related fields. J. Struct. Biol. *116*, 190–199.

Fujiwara, I., Vavylonis, D., and Pollard, T.D. (2007). Polymerization kinetics of ADP- and ADP-Pi-actin determined by fluorescence microscopy. Proc. Natl. Acad. Sci. USA *104*, 8827–8832.

Hayward, S., and Berendsen, H.J.C. (1998). Systematic analysis of domain motions in proteins from conformational change: new results on citrate synthase and T4 lysozyme. Proteins *30*, 144–154.

Heintz, D., Kany, H., and Kalbitzer, H.R. (1996). Mobility of the N-terminal segment of rabbit skeletal muscle F-actin detected by 1H and 19F nuclear magnetic resonance spectroscopy. Biochemistry *35*, 12686–12693.

Holmes, K.C., Popp, D., Gebhard, W., and Kabsch, W. (1990). Atomic model of the actin filament. Nature *347*, 44–49.

Jones, T.A., Zou, J.Y., Cowan, S.W., and Kjeldgaard, M. (1991). Improved methods for building protein models in electron density maps and the location of errors in these models. Acta Crystallogr. A *47*, 110–119.

Kabsch, W., Mannherz, H.G., Suck, D., Pai, E.F., and Holmes, K.C. (1990). Atomic structure of the actin:DNase I complex. Nature *347*, 37–44.

Khaitlina, S.Y., Moraczewska, J., and Strzelecka-Golaszewska, H. (1993). The actin/actin interactions involving the N-terminus of the DNase-I-binding loop are crucial for stabilization of the actin filament. Eur. J. Biochem. *218*, 918–920.

Klenchin, V.A., Khaitlina, S.Y., and Rayment, I. (2006). Crystal structure of polymerization-competent actin. J. Mol. Biol. *362*, 140–150.

Klenchin, V.A., Allingham, J.S., King, R., Tanaka, J., Marriott, G., and Rayment, I. (2003). Trisoxazole macrolide toxins mimic the binding of actin-capping proteins to actin. Nat. Struct. Biol. *10*, 1058–1063.

Koradi, R., Billeter, M., and Wüthrich, K. (1996). MOLMOL: a program for display and analysis of macromolecular structures. J. Mol. Graph. *14*, 51–55, 29–32.

Laki, K., Maruyama, K., and Kominz, D.R. (1962). Evidence for the interaction between tropomyosin and actin. Arch. Biochem. Biophys. *98*, 323–330.

Liu, X., Shu, S., Hong, M.S., Levine, R.L., and Korn, E.D. (2006). Phosphorylation of actin Tyr-53 inhibits filament nucleation and elongation and destabilizes filaments. Proc. Natl. Acad. Sci. USA *103*, 13694–13699.

Lorenz, M., Popp, D., and Holmes, K.C. (1993). Refinement of the F-actin model against X-ray fiber diffraction data by the use of a directed mutation algorithm. J. Mol. Biol. *234*, 826–836.

Matsuura, Y., Stewart, M., Kawamoto, M., Kamiya, N., Saeki, K., Yasunaga, T., and Wakabayashi, T. (2000). Structural basis for the higher Ca(2+)-activation of the regulated actin-activated myosin ATPase observed with *Dictyostelium*/*Tetrahymena* actin chimeras. J. Mol. Biol. *296*, 579–595.

Narita, A., Yasunaga, T., Ishikawa, T., Mayanagi, K., and Wakabayashi, T. (2001). Ca(2+)-induced switching of troponin and tropomyosin on actin filaments as revealed by electron cryo-microscopy. J. Mol. Biol. *308*, 241–261.

Narita, A., and Maéda, Y. (2007). Molecular determination by electron microscopy of the actin filament end structure. J. Mol. Biol. *365*, 480–501.

Noda, K., Nakamura, M., Nishida, R., Yoneda, Y., Yamaguchi, Y., Tamura, Y., Nakuamura, H., and Yasunaga, T. (2006). Atomic model construction of protein complexes from electron micrographs and visualization of their 3D structure using VR system. J. Plasma Phys. *72*, 1037–1040.

Noguchi, T.Q., Kanzaki, N., Ueno, H., Hirose, K., and Uyeda, T.Q. (2007). A novel system for expressing toxic actin mutants in Dictyostelium and purification and characterization of a dominant lethal yeast actin mutant. J. Biol. Chem. *282*, 27721–27727.

Nolen, B.J., and Pollard, T.D. (2007). Insights into the influence of nucleotides on actin family proteins from seven structures of Arp2/3 complex. Mol. Cell *26*, 449–457.

Nonomura, Y., Katayama, E., and Ebashi, S. (1975). Effect of phosphates on the structure of the actin filament. J. Biochem. *78*, 1101–1104.

Nyman, T., Schüler, H., Korenbaum, E., Schutt, C.E., Karlsson, R., and Lindberg, U. (2002). The role of MeH73 in actin polymerization and ATP hydrolysis. J. Mol. Biol. *317*, 577–589.

Oda, T., Iwasa, M., Aihara, T., Maéda, Y., and Narita, A. (2009). The nature of the globular- to fibrous-actin transition. Nature *457*, 441–445.

Otterbein, L.R., Graceffa, P., and Dominguez, R. (2001). The crystal structure of uncomplexed actin in the ADP state. Science *293*, 708–711.

Pettersen, E.F., Goddard, T.D., Huang, C.C., Couch, G.S., Greenblatt, D.M., Meng, E.C., and Ferrin, T.E. (2004). UCSF Chimera—a visualization system for exploratory research and analysis. J. Comput. Chem. *25*, 1605–1612.

Rickard, J.E., and Sheterline, P. (1986). Cytoplasmic concentrations of inorganic phosphate affect the critical concentration for assembly of actin in the presence of cytochalasin D or ADP. J. Mol. Biol. *191*, 273–280.

Rosenthal, P.B., and Henderson, R. (2003). Optimal determination of particle orientation, absolute hand, and contrast loss in single-particle electron cryomicroscopy. J. Mol. Biol. *333*, 721–745.

Rould, M.A., Wan, Q., Joel, P.B., Lowey, S., and Trybus, K.M. (2006). Crystal structures of expressed non-polymerizable monomeric actin in the ADP and ATP states. J. Biol. Chem. *281*, 31909–31919.

Saeki, K., Sutoh, K., and Wakabayashi, T. (1996). Tropomyosin-binding site(s) on the Dictyostelium actin surface as identified by site-directed mutagenesis. Biochemistry *35*, 14465–14472.

Spudich, J.A., and Watt, S. (1971). The regulation of rabbit skeletal muscle contraction. I. Biochemical studies of the interaction of the tropomyosin-troponin complex with actin and the proteolytic fragments of myosin. J. Biol. Chem. *246*, 4866–4871.

Storoni, L.C., McCoy, A.J., and Read, R.J. (2004). Likelihood-enhanced fast rotation functions. Acta Crystallogr. D Biol. Crystallogr. *60*, 432–438.

Vorobiev, S., Strokopytov, B., Drubin, D.G., Frieden, C., Ono, S., Condeelis, J., Rubenstein, P.A., and Almo, S.C. (2003). The structure of nonvertebrate actin: implications for the ATP hydrolytic mechanism. Proc. Natl. Acad. Sci. USA *100*, 5760–5765.

Wriggers, W., and Schulten, K. (1999). Investigating a back door mechanism of actin phosphate release by steered molecular dynamics. Proteins *35*, 262–273.

Yasunaga, T., and Wakabayashi, T. (1996). Extensible and object-oriented system Eos supplies a new environment for image analysis of electron micrographs of macromolecules. J. Struct. Biol. *116*, 155–160.

Yasunaga, T., and Wakabayashi, T. (2008). Evaluation of a 2k CCD camera with an epitaxially grown CsI scintillator for recording energy-filtered electron cryo-micrographs. J. Electron Microsc. (Tokyo) *57*, 101–112.

Yonekura, K., Maki-Yonekura, S., and Namba, K. (2003). Complete atomic model of the bacterial flagellar filament by electron cryomicroscopy. Nature *424*, 643–650.